ROYAL SOCIETY OF CHEMISTRY

Check for updates

Electrochemical nanosensors using MXene-carbon dot modified screen-printed carbon electrodes for creatinine detection in serum samples

Poornima Bhatt,[ab] Monika Chhillar,[c] Anup Singh,[de] Deepak Kukkar, [iD] *[ab] Ashok Kumar,[e] Ashok Kumar Yadav,[c] Jaskiran Kaur[ce] and Manil Kukkar*[f]

An innovative electrochemical (EC) nanosensor utilizing screen-printed carbon electrodes (SPCEs) functionalised with MXenes ($Ti_3C_2T_x$) and carbon dots (CDs) has been developed for the ultrasensitive sensing of creatinine in phosphate-buffered saline (PBS) and human serum samples. This novel SPCE@MXene@CDs configuration significantly enhanced redox signals, achieving excellent sensitivity with a 0.016 mg dL^{-1} detection limit. The electrical conductivity of the SPCE@MXene@CDs sensor was enhanced by systematically optimizing four key parameters: scan rate, number of scan cycles, pH of the PBS buffer, and CD concentration during fabrication. The nanosensor demonstrated outstanding selectivity with no interference from common metabolites (*e.g.*, glucose, urea, ascorbic acid, glutathione, bovine serum albumin, globulin, bilirubin, gentamicin, vancomycin, arginine, and histidine) and electrolytes (Ca^{2+}, Mg^{2+}, PO_4^{3-}, and SO_4^{2-}). Additionally, the nanosensor demonstrated a high correlation with the standard Jaffe method (R^2 = 0.99) for creatinine detection in ultra-low serum volumes of 5 μL (n = 89). The nanosensor exhibited remarkable stability, retaining 97.8% of its initial response after 15 days, along with excellent reproducibility confirmed by overlapping cyclic voltammetry cycles, underscoring its reliability for practical creatinine detection. Our research findings underscore the potential of this nanosensor for rapid, highly sensitive, and point-of-care creatinine monitoring in complex biological environments.

1. Introduction

Chronic kidney disease (CKD) is an escalating medical concern globally, affecting a vast number of individuals around the world.[1] CKD is increasingly recognized as a key factor in global death rates, with its prevalence increasing due to the growing incidence of diabetes, hypertension, and the aging population.[2] Global bodies like the International Society of Nephrology and the World Health Organization are actively engaged in increasing awareness, advancing screening techniques, and promoting fair access to CKD treatment globally.[3,4] However, more coordinated efforts are needed to address this crisis through better education on risk factors, earlier diagnosis, and the development of affordable, effective treatments.

Creatinine (CR), the most extensively sought out CKD biomarker, is a small molecule (113 Da).[5] It is produced through the non-enzymatic transformation of creatine or phosphocreatine into phosphocreatinine, which is subsequently dephosphorylated.[6] It serves as an endogenous filtration marker, reflecting the kidneys' metabolic function and is frequently utilized in medical settings to assess the glomerular filtration rate (GFR).[7,8] CR levels in CKD patients may exceed the normal values (0.7–1.3 mg dL^{-1} in men and 0.5–1.1 mg dL^{-1} in women), depending on the extent of kidney impairment.[9,10] Several methods are used clinically for CR determination, each with pros and cons. The Jaffe reaction, commonly used due to its simplicity and low cost, suffers from poor specificity as it reacts with other substances like glucose and proteins.[11,12] Enzymatic assays are more specific but are expensive and require specialized reagents.[13] Additionally, isotope dilution mass spectrometry and high-performance liquid chromatography are costly, time-consuming, and require skilled technicians.[14] Despite their advantages, the aforementioned methods face issues like sample variations and potential interferences. Given the

a Department of Biotechnology, Chandigarh University, Gharuan, Mohali 140413, Punjab, India. E-mail: dr.deepakkukkar@gmail.com, dr.manilkukkar@gmail.com

b University Centre for Research and Development, Chandigarh University, Gharuan, Mohali 140413, Punjab, India

c Department of Experimental Medicine and Biotechnology, Post Graduate Institute of Medical Education and Research, Sector 12, Chandigarh, India

d Department of Physics, Chandigarh University, Gharuan, Mohali 140413, Punjab, India

e Department of Applied Sciences, National Institute of Technical Teachers Training and Research, Chandigarh 160019, India

f University of Novi Sad, BioSense Institute, 21000 Novi Sad, Serbia

limitations of current CR detection methods, there is a pressing need to develop a nanosensor for reliable CR detection in human samples with minimal sample requirements and capabilities for miniaturization.

Electrochemical (EC) sensing offers notable benefits for CR detection compared to the abovementioned methods. It provides high sensitivity and selectivity, allowing for the accurate measurement of low CR concentrations.[15] The technology is characterized by fast response times, enabling quick results, real-time monitoring, cost-efficacy, and feasibility for on-site testing.[16] Additionally, it often requires minimal sample preparation and has low power consumption, making it practical for analytical applications.[17] Incorporating MXenes and carbon dots (CDs) into EC sensors enhances sensitivity, increases surface area, and improves electron transfer.[18] MXenes are a distinct group of two-dimensional compounds made from transition metal carbides, nitrides, or carbonitrides.[19] These materials typically follow a general composition involving early transition metals (like Ti, V, or Cr), combined with carbon or nitrogen atoms, and surface terminations such as –OH, –O, or –F. A typical MXene sheet is composed of multiple atomic layers—commonly 3, 5, or 7—depending on its structure type, such as M_2X, M_3X_2, or M_4X_3.[20] These materials boost selectivity and stability and enable lower detection limits (DL) and faster response times, making sensors more effective and reliable.

Numerous studies have explored CR measurement using advanced electrochemical techniques, with a focus on nanomaterial-modified sensors for improved sensitivity, selectivity, and device integration.[21–23] For instance, a highly sensitive system for CR detection was constructed by functionalizing a screen-printed carbon electrode (SPCE) with Cu_2O nanoparticles (NPs) incorporated into a molecularly imprinted polymer layer.[24] This platform achieved a sensitivity of 2.16 A M^{-1} cm^{-2} and a DL of 22 nM. Another report described a platinum microelectrode array (Pt-MEA)-based EC sensor for CR detection.[25] Herein, Cu^{2+} ions interact with CR to yield a redox-active species. The developed nanosensor was able to analyze CR across a range spanning from 0.00 to 5.00 mM, with a DL of 0.059 mM. Later, a SPCE modified with MXene-gold nanomaterials (NMs) was designed for rapid CR detection.[26] The $Ti_3C_2T_X$ MXene with *in situ* reduced gold NPs enabled efficient enzyme immobilization. CR oxidation catalyzed by chitosan-embedded enzymes generated H_2O_2, which was subsequently detected electrochemically using Prussian blue. The sensor detected CR across a range of 0.03 to 4.0 mM, achieving a DL of 0.01 mM and recovery rates between 96.8% and 103.7%. Of late, a 3D printed Co-MOF–MXene-carbon black ink electrode was developed for EC analysis of blood CR, achieving a DL of 0.005 μM and a sensitivity of 1.1 μA $μM^{-1}$ cm^{-2}.[27]

In spite of the advancement in electrochemical sensing techniques, the reported literature on EC CR measurements suffers from several shortcomings. These include insufficient sensitivity for low CR concentrations, poor selectivity, reduced temporal stability, high fabrication costs of the sensing materials, and limited applicability in complex biological matrices. Improvements are required regarding sensitivity, stability, cost-efficacy,

and analyte detection in low sample volumes. To address these research gaps, we developed a cutting-edge EC sensing technique employing MXenes (Ti_3C_2X) and CDs in conjunction with a SPCE and cyclic voltammetry (CV) for detecting CR in phosphate-buffered saline (PBS, pH 7) and human serum from both healthy individuals and CKD patients. This innovative approach harnesses the distinctive properties of MXenes and CDs to enable accurate CR measurement in very small volumes of human serum (5 μL). Henceforth, our developed nanosensor demonstrates a notable advancement over previously reported methods.

2. Experimental design

2.1. Materials

Laboratory-grade compounds, including $CaCl_2$ (99.95%), $MgCl_2$ (99.9%), H_2SO_4 (98%), HF (50 wt%), and HCl (99%, 11.6 N), were provided by Sigma Chemicals, Missouri, USA. CR was sourced through Loba Chemie Limited, India. Lithium chloride anhydrous (LiCl, 98% grade) was obtained from Honeywell Specialty Chemicals, Seelze, Germany. Other chemicals such as glucose (98.8%), $NaHCO_3$ (99%), urea (98.9%), CH_3COOH (99.8%), sucrose (98.9%), bovine serum albumin (BSA) (98%), ascorbic acid (99%), and glutathione (GSH) (98%) were supplied by Spectrum Chemical Corporation, Mumbai, India. MAX phase was sourced from Nanochemazone, Kurukshetra, Haryana, India. A Milli-Q EQ 7000 system provided deionized (DI) water with a resistivity of 18.2 MΩ cm. Polytetrafluoroethylene (PTFE) filter papers (0.8 μm, 0.2 μm and 2 μm) were obtained from Carl Roth, Germany. Additional chemicals, including Na_2SO_4 (98.9%), KCl (98.9%), KH_2PO_4 (98.95%), and NaCl (98.7%), were purchased from Sisco Research Limited, Mumbai, India.

2.2. Methodology

2.2.1. Synthesis of carbon dots (CDs). A sophisticated microwave-assisted technique was employed to prepare CDs, using sucrose as the carbon precursor.[28,29] The complete synthesis method for CDs is thoroughly outlined in our earlier publication,[30] as well as referenced in the patent application titled "Carbon dot-graphene oxide-based luminescent nanosensor" (Patent application number – 202411032295).

2.2.2. Synthesis of MXenes. Layered MXene ($Ti_3C_2T_X$) nanosheets were synthesized through a hydrochloric acid–hydrofluoric acid (HCl–HF) etching method.[31] The process commenced by adding 9 mL of DI water into a 125 mL high-density polyethylene (HDPE) Nalgene container (Thermo Fisher Scientific, Massachusetts, USA), which was then clamped to a hot plate. 18 mL of 12 M HCl (37%) was added, and stirring was gradually increased to 200 revolutions per minute (RPM). Afterwards, 3 mL of 28.4 M (48%) HF was added to the mixture under controlled conditions, followed by supplementation with MAX phase powder (Ti_3AlC_2) at a rate of 1 g min^{-1}.[32] The stirring speed was increased to 400 RPM, and the system was maintained at 35 °C for 24 hours. Afterwards, the multi-layered MXene ($Ti_3C_2T_X$) underwent several washing steps using DI water. Each cycle included centrifugation at 3234 RCF for

5 minutes, and the process continued until the suspension reached a neutral pH. The neutralized MXene powder was then subjected to vacuum filtration with a 0.1 μm PTFE membrane. For delamination, 1 g of LiCl was mixed with 25 mL of DI water in an HDPE container, and the etched MXene powder was added along with an additional 25 mL of DI water. The resulting solution was agitated at 400 RPM and maintained at 65 °C for 1 hour under an argon atmosphere. Subsequent washing was performed using DI water, with centrifugation times gradually increasing from 5 minutes to 20 minutes with an increment of 5 min, each at 3234 RCF. Initially, the supernatant was clear, but it darkened with continued washing. After using 100 mL of water, MXene clay began to form, which swelled with further washing. Manual shaking with a glass rod and vortex mixing was used to dissolve the clay between washes. The dispersion was moved to a 50 mL centrifuge tube and vortexed for around 30 minutes. Afterward, centrifugation was carried out at 2380 RCF for 30 minutes to isolate the one-to-several-layer MXene nanosheets. A final MXene concentration of 3 mg mL^{-1} was achieved at the end of the centrifugation and washing procedure. The resulting dispersion was purged with argon and stored at room temperature (RT) for future use.

2.2.3. Functionalization of the SPCE using MXene@CDs. A 10 μL suspension of MXene (1.0 mg dL^{-1}) was introduced to the SPCE surface and left to evaporate naturally at RT overnight. The CV response of the MXene-modified SPCE (SPCE@MXene) was measured in a 0.1 M PBS solution at pH 7. This reaction was performed within a potential window of −1.0 V to 1.0 V relative to Ag/AgCl, using a 50 mV s^{-1} scanning rate. Repetitive scans were performed until consistent peak currents appeared at the anodic and cathodic potentials. Subsequently, 10 μL of CDs (average diameter = 5 nm) was dropcast onto the MXene-modified SPCE. The electrode was then allowed to air-dry for 5 hours at RT after being rinsed with DI water. The final modified electrode was referred to as SPCE@MXene@CDs.

2.2.4. Standardization of experimental conditions. To achieve optimal performance of the SPCE@MXene@CDs sensor, four essential parameters were systematically examined: scan rate, number of scan cycles, pH, and CD concentration. Various scan rates (5–70 mV s^{-1}) were tested to evaluate electrode kinetics and electron transfer efficiency. The number of scan cycles was adjusted from 2 to 20 cycles to ensure uniform deposition of MXene and CDs on the SPCE surface. pH optimization was carried out using PBS buffer solutions across the range of 3–10 to determine the most favourable conditions for electrochemical response. Additionally, the CD concentration (0.1–5 mg dL^{-1}) was optimized to enhance surface modification and signal intensity. These parameters were systematically fine-tuned to establish the most effective conditions for nanosensor development.

2.2.5. Electrochemical sensing of CR. For CR sensing, a stock solution of CR was prepared with PBS (pH = 7) at 5 mg dL^{-1} by dissolving 1 mg of CR in 20 mL of 0.1 M PBS. This solution was then diluted to create working concentrations ranging from 0.001 to 5.0 mg dL^{-1}. Next, 5 μL of these CR solutions each was applied to the SPCE@MXene@CDs. After air-drying at RT for three hours,

the EC redox signals of the CR-treated SPCE@MXene@CDs (SPCE@MXene@CDs@CR) were recorded using CV in PBS (0.1 M, pH 7) over 12 cycles. Each measurement was repeated three times using a scan rate of 50 mV s^{-1}, covering a voltage span from −1.0 V to 1.0 V relative to the Ag/AgCl reference electrode.

The specificity of the SPCE@MXene@CDs sensor for CR was tested against potential interferents like urea, glucose, potassium (K$^+$), calcium (Ca^{2+}), AA, BSA, sulphate (SO$_4{}^{2-}$), GSH, globulin, bilirubin, gentamicin, vancomycin, arginine, histidine and magnesium (Mg^{2+}). All interfering molecules were tested at their physiological concentrations to closely mimic real serum conditions. This ensures the selective response of the nanosensor for CR, minimizing the risk of false positives or negatives and demonstrating its reliability for practical applications. A mixture containing 10 μL each of CR (1.2 mg dL^{-1}), AA (10 mg dL^{-1}), BSA (3.0 mg dL^{-1}), globulin (0.1 mg dL^{-1}), bilirubin (0.2 mg dL^{-1}), gentamicin (1 mg dL^{-1}), vancomycin (2 mg dL^{-1}), arginine (20 mg dL^{-1}), histidine (1 mg dL^{-1}), GSH (90.1 mg dL^{-1}), urea (24 mg dL^{-1}), glucose (15 mg dL^{-1}), Ca^{2+} (10.5 mg dL^{-1}), Mg^{2+} (2.5 mg dL^{-1}), K$^+$ (22 mg dL^{-1}), and sulphate (2.88 mg dL^{-1}) in PBS (0.1 M, pH 7) was prepared. The resulting solutions were air-dried on the SPCE@MXene@CDs for 3 hours, both individually and in combination. The EC signals from these samples were then compared to those from CR alone.

The thickness of the modified layer on the working electrode surface of the SPCE@MXene@CDs nanosensor was estimated using the mass–density–area relationship, as given in the following equation:

$$t = \frac{m}{\rho \cdot A} \tag{1}$$

where t is the film thickness (m), m is the deposited mass (kg), ρ is the density of the coating material (kg m^{-3}), and A is the electrode surface area (m^2). For the present work, 5 μL of MXene and 5 μL of CD suspensions (1 mg dL^{-1}) were dropcast sequentially onto the working electrode. The working electrode diameter was 3 mm, giving an area of approximately 7.07 mm^2.

The analytical performance of the SPCE@MXene@CDs EC nanosensor was determined through computation of detection limit (DL) and quantification limit (QL). These values were determined using the below mentioned mathematical formulas:[33–35]

$$DL = \frac{3\sigma}{K} \tag{2}$$

$$QL = \frac{10\sigma}{K} \tag{3}$$

Here, σ refers to the standard deviation of the intercept, while K represents the slope of the linear standard curve.

The real-world performance of the SPCE@MXene@CDs sensor was evaluated using human serum samples ($n = 89$), including 22 samples collected from the Post Graduate Institute of Medical Education & Research (PGIMER), Chandigarh, and 67 samples obtained from HICARE Multispeciality Hospital, Ludhiana. The serum samples were kept at −80 °C and examined within 24 hours. A 5 μL aliquot of each serum sample was applied to the SPCE@MXene@CDs using the same method

as for calibration standards. The redox EC signals were recorded using CV, following the same procedure applied to the PBS-based CR samples.

2.2.6. Quantitative and diagnostic instruments. To fabricate CDs, a Samsung 32 L Microwave Oven (Model MC32A7056QT/TL, Republic of Korea) was used. EC experiments were performed over a SPCE from Zensor, Pune, India. In this setup, carbon acted as both the working and counter electrode, while Ag/AgCl functioned as the reference electrode. A potentiostat (SP-150, BioLogic SAS, France) controlled by NOVA 2.1 software was used for EC analysis. The nanostructures of bare SPCE, SPCE@MXene, and SPCE@MXene@CDs were studied with an HR-TEM system (200 kV JEOL JEM 2100, Tokyo, Japan). A scanning electron microscope (SEM) (JEOL JSM-IT500, Japan) was used for the energy-dispersive X-ray spectroscopy (EDX) investigation of the MAX phase (Ti_3AlC_2), delaminated MXene sheets (Ti_3C_2X), and the modified SPCEs. A JEOL JSM-IT710 HR-SEM, Japan was employed to analyse the structural and morphological features of Ti_3AlC_2 and delaminated Ti_3C_2X. The samples were fabricated by depositing MXene flakes from a diluted solution onto a silicon substrate. Powder samples were utilized for the MAX phase and etched multilayer MXenes. HR-SEM provided high-resolution imaging for analyzing the surface structure, layer morphology, and delamination features of the samples. X-ray diffraction (XRD) profiles of the Max phase and delaminated MXene sheets were analysed using a Bruker XRD D8 ADVANCE ECO, Japan. Moreover, the surface functional groups present on CDs, MXene, bare SPCE, SPCE@MXene, and SPCE@MXene@CDs were examined using FTIR spectroscopy (Thermo Scientific Nicolet iS10, USA).

3. Results and discussion

3.1. Formation and evaluation of CDs and MXene

The prepared CD suspension displayed green fluorescence under UV light (365 nm) with excitation peaking at 390 nm and emission observed at 453 nm (Fig. S1A and B). Microscopic analysis of CDs using HRTEM and SEM-EDX revealed uniform spherical morphology, typically measuring around 5 nm in diameter (Fig. S1C–E). The XRD pattern of the CDs corresponded to the characteristic diffraction profile of graphitic carbon (JCPDS26-1076) (Fig. S1F).[36] These XRD results suggested the amorphous characteristics of CDs. The synthesized CDs exhibited a zeta potential of −19.3 mV, indicating good colloidal dispersion stability (Fig. S1G). FTIR-based structural elucidation of CDs displayed a wide OH band near 3460 cm^{-1} and C–H and carboxylate (COO^-) stretching at 2425 and 1384 cm^{-1}, respectively, along with signals corresponding to C=O and C=C groups at 1767 cm^{-1} and 1639 cm^{-1}. These bands contribute to the CDs' aqueous solubility (Fig. S1H).[37,38] For a detailed explanation of the synthesis and characterization of CDs, please refer to our previously published report.[39]

The synthesized MXene ($Ti_3C_2T_X$) nanosheets were characterized by several spectroscopic and microscopic methods. Synthesis of MXenes from the MAX phase induces a
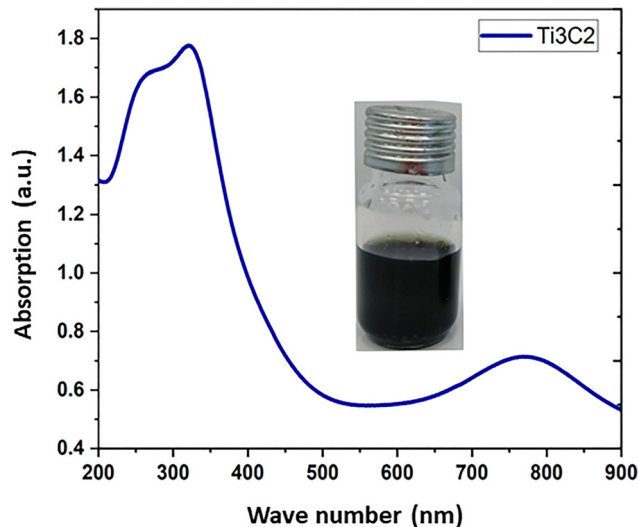

Fig. 1 UV-Visible characteristics of delaminated MXene sheets (Ti_3C_2X).

pronounced and observable colour shift from grey metallic colour to deep greenish-black colour. MXenes exhibit distinct optical characteristics in the sense that their light absorption, reflection, and scattering properties are strongly influenced by their unique 2D structure, chemical composition, and surface terminations (*e.g.*, –F, –OH, and –O). While MAX phases typically exhibit a grey hue and the dispersion of the delaminated MXene nanosheets in water yielded a black solution. However, at concentrations <0.5 ng mL^{-1}, the aqueous suspension appears green (inset of Fig. 1). The UV-visible absorption spectrum of MXene nanosheets showed a well-resolved characteristic peak at 780 nm, which corresponds to delaminated nanosheets (Fig. 1).[40] Optical absorption at 0.8 eV is attributed to dipole surface plasmons, while absorption at 1.7 eV corresponds to transverse surface plasmons. The inter-band electronic transitions occur below 1.6 eV and above 3 eV.[41] The morphology of the MAX phase and delaminated few-layered MXene was examined by HR-SEM (Fig. 2A–C). HR-SEM images illustrated a bulk structure of the MAX phase with stacked layers, while the delaminated material presented few-layered nanosheet morphology. EDX analysis, including elemental mapping, highlighted characteristic peaks for Ti, Al, and C elements for the Max phase (Fig. 2D–F). On the other hand, Ti, C, F and Cl elements were observed for delaminated layered MXene nanosheets in the EDX analysis (Fig. 2G–I). EDX analysis confirmed the purity of the delaminated layered nanosheets, showing the absence of Al in the elemental composition. These findings suggested the successful assembly of the desired MXenes. Delamination of the MAX phase to yield MXene was further assessed using XRD analysis. The (002) peak, corresponding to the crystallographic plane of MXene, remained the dominant feature after the etching, intercalation, and delamination of the MAX phase (Fig. 3A). Additionally, the broadening and shift in the (002) peak from delaminated nanosheets indicate the reduction in the thickness of the $Ti_3C_2T_X$ MXene layers and an increase in d-spacing.

The FTIR analysis was performed for the delaminated MXene nanosheets by using the KBr method as illustrated in
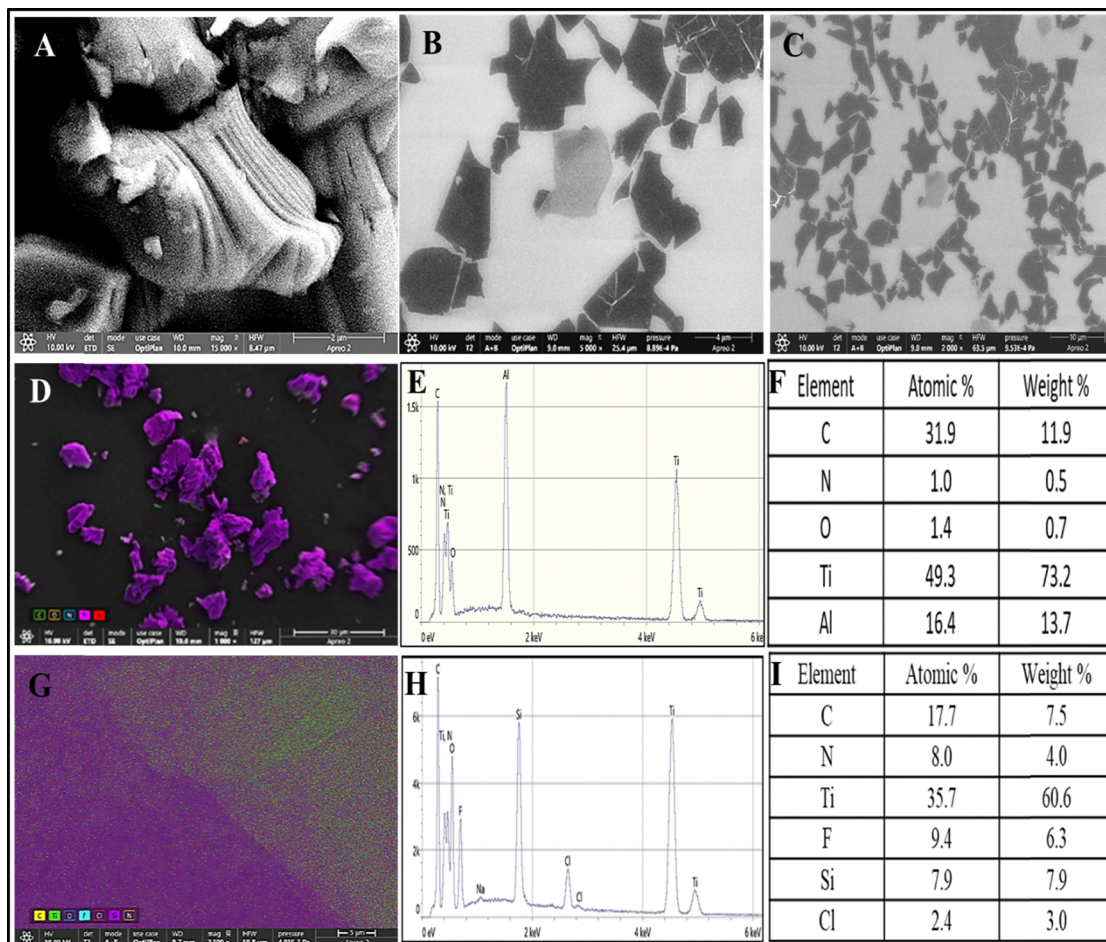
Fig. 2 Microscopic characterization of MXene: HR–SEM for (A) the Max phase (Ti_3AlC_2) and (B) and (C) delaminated MXene sheets (Ti_3C_2X); EDS analysis: (D) EDS image, (E) EDS mapping, and (F) elemental composition of the Max phase (Ti_3AlC_2X); (G) EDS image, (H) EDS mapping, and (I) elemental composition of delaminated MXene sheets (Ti_3C_2X).

Fig. 3B. The FTIR characterization of $Ti_3C_2T_X$ features two specific regions: a higher wavenumber range (4000–1400 cm^{-1}) associated with water and carbon-related vibrations and a lower region (1400–400 cm^{-1}) representing the characteristic

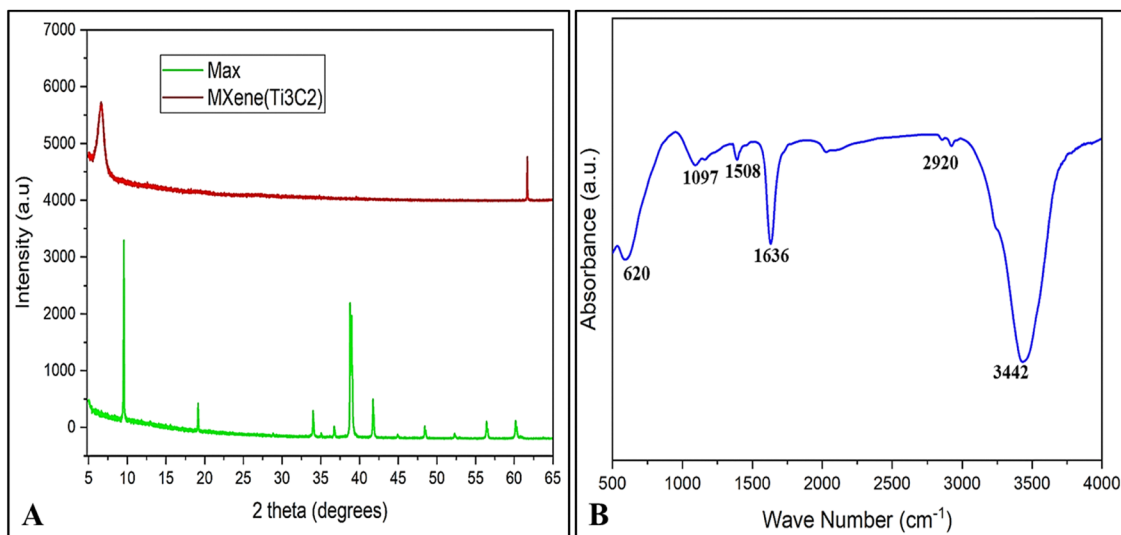**Fig. 3** Characteristics study: (A) XRD of the Max phase (Ti_3AlC_2) and delaminated MXene sheets (Ti_3C_2X) and (B) FTIR of delaminated MXene sheets (Ti_3C_2X).

fingerprint zone.[42,43] The broad absorption bands corresponding to O–H stretching and O–H bending were observed at 3600–3200 and 1500–1300 cm^{-1}, respectively. Significant carbon-related vibrations, such as C–H stretching (3000–2800 cm^{-1}), C–O stretching (1750–1700 cm^{-1}), and C–H bending (1500–1400 cm^{-1}), were also identified.[44–46] The fingerprint region depicts the C–F stretching, Ti–F bending, Ti–O bending, and Ti–C stretching at 1400–1000, 750–700, 650–550, and 450–350 cm^{-1}, respectively. Additionally, bending vibrations associated with C–C bonds were observed between 500 and 400 cm^{-1}.[42,44–46]

3.2. Formation and assessment of the CDs@MXene-modified SPCE

FTIR analysis was performed to examine the comparative structural modifications in the bare SPCE, SPCE@MXene, and SPCE@MXene@CDs (Fig. 4A). The SPCE@MXene exhibited an extensive absorption signal near 3668 cm^{-1}, suggestive of hydroxyl bond stretching.[47] The abovementioned C–F stretching, Ti–F bending, Ti–O bending, and Ti–C stretching vibrations confirmed the successful integration of MXene onto the surface of the SPCE. The SPCE@MXene@CDs spectrum exhibited a wide absorption band around 3760 cm^{-1}, originating from O–H stretching.[37] The bands at 1680 and 1498 cm^{-1} showed the presence of C=O and C=C bonds, respectively, confirming the attachment of CDs over the SPCE@MXene composite.[38] Overall, the FTIR observations highlight the effective formation of a composite electrode with distinct chemical functionalities. The sequential modifications of the SPCE enhance its surface properties, making the electrode suitable for CR quantification.

Next, HRTEM analysis of bare SPCE, SPCE@MXene, and SPCE@MXene@CDs was performed to verify the integrity and interaction of SPCE with the CDs and MXene (Fig. 4B–D). HRTEM of bare SPCE revealed a relatively smooth and uniform surface, characteristic of their appearance (Fig. 4B). Fig. 4C illustrates the presence of creases in the MXene layer, indicating a high surface area-to-volume ratio. A broader surface area facilitates the fixation of CDs over the MXene surface. This attachment is driven by forces such as electrostatic interactions, hydrogen bonds, and π–π stacking between MXene and
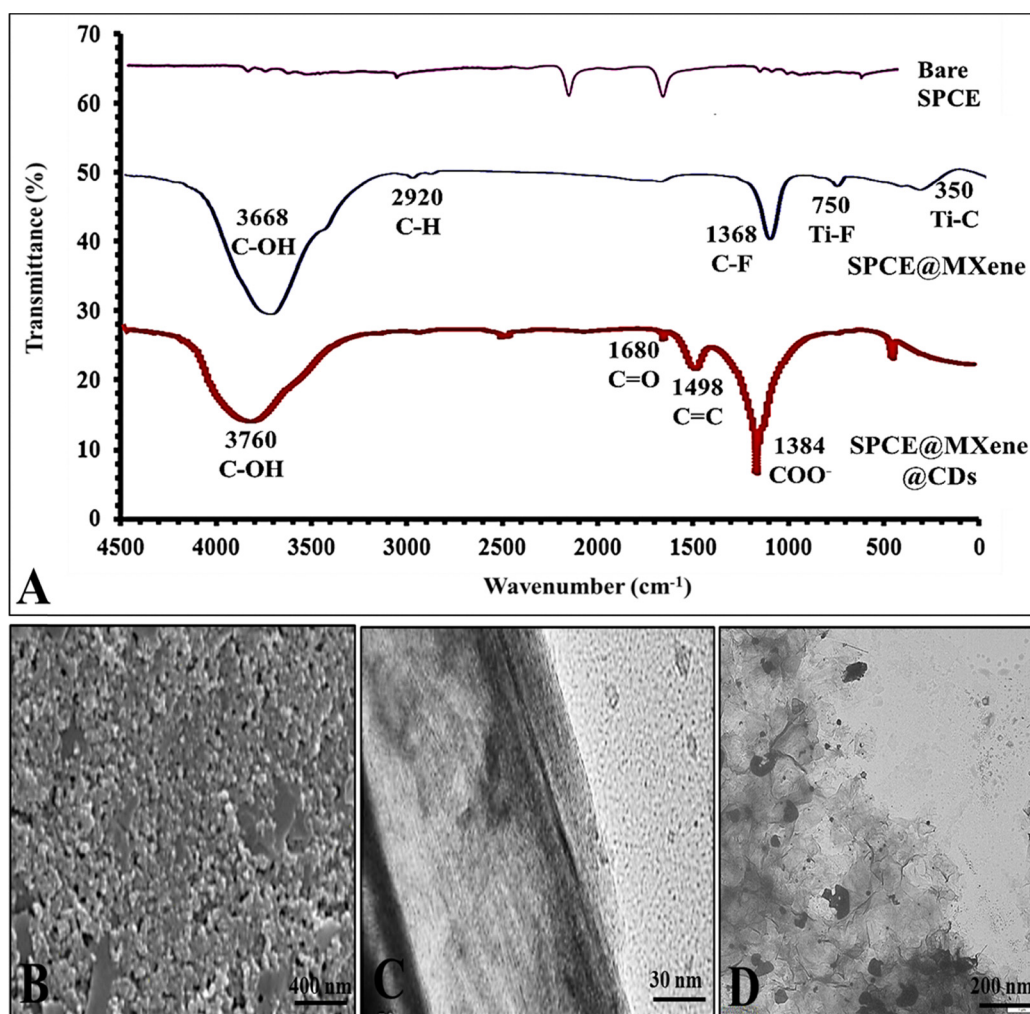

Fig. 4 SPCE characteristics study: (A) FTIR spectra of bare SPCE, SPCE@MXene, and SPCE@MXene@CDs and (B) HRTEM images of bare SPCE, SPCE@MXene, and SPCE@MXene@CDs.

CDs' functional groups. These interactions ensured stable attachment, promoting the formation of a robust MXene-CD composite. This characteristic enhances the integration of CDs on the SPCE/MXene surface, improving charge conductivity. The modified two-dimensional thin layer of SPCE@MXene@CDs exhibited a folded/crumpled morphology with evenly distributed CDs (Fig. 4D). The deposition of the MXene layer over the surface of SPCE produced minimal microscopic tears or distortions to suggest uniform dispersion of the sensing surface. The morphology and elemental composition of bare SPCE, SPCE@MXene and SPCE@MXene@CDs were also analysed using SEM-EDX (Fig. S2A–D). The SEM image of bare SPCE (Fig. S2A) reveals a smooth and uniform surface. In contrast, SPCE@MXene (Fig. S2B) shows a layered, wrinkled structure, confirming the successful integration of MXene. The SEM image of SPCE@MXene@CDs (Fig. S2C) exhibits a textured surface with uniformly distributed NPs, indicating effective CD immobilization and enhanced surface modification. The thickness of the SPCE@MXene@CDs film was approximately 8.25 nm, as calculated using eqn (1). This theoretical value showed excellent agreement with the SEM analysis, which revealed an average coating thickness of 8.2 nm (Fig. S2C). The close correlation between the calculated and experimental results confirms the uniformity and reproducibility of the film deposition process. Elemental analysis of C and O in bare SPCE, SPCE@MXene, and SPCE@MXene@CDs highlighted the surface composition changes during each modification step (Fig. S2D). The weight% of C and O content in SPCE@MXene@CDs increased to 38.2 and 20.3%, respectively, compared to 17.7 and 0% in SPCE@MXene. The subsequent rise in C and O content in SPCE@MXene@CDs indicates the successful incorporation of CDs onto the MXene-modified SPCE, introducing additional functional sites. The rise in carbon content improves the SPCE's conductivity, surface activity, and charge transfer, enhancing its performance in sensing applications. Overall, the SEM-EDX analysis revealed uniform modification in the morphology and chemical functionality of the SPCE across each modification step.

To enhance the performance of the SPCE@MXene@CDs sensor, four key parameters were systematically optimized as mentioned in Section 3. Fig. 5 illustrates the average peak currents generated due to the interaction of CDs on SPCE@MXene. The peak current increased gradually when the scan rate varied between 5 and 50 mV s^{-1} (Fig. 5A). This observation can be attributed to enhanced electron transfer rate and improved interaction between the electrode surface and the electroactive species. However, at scan rates exceeding 60 mV s^{-1}, a decline in peak current was observed, which can be a consequence of diffusion limitations and increased capacitive current, reducing the efficiency of faradaic processes. Additionally, at higher scan rates, the shorter duration for redox reactions may contribute to the decrease in peak current.[48] Based on these
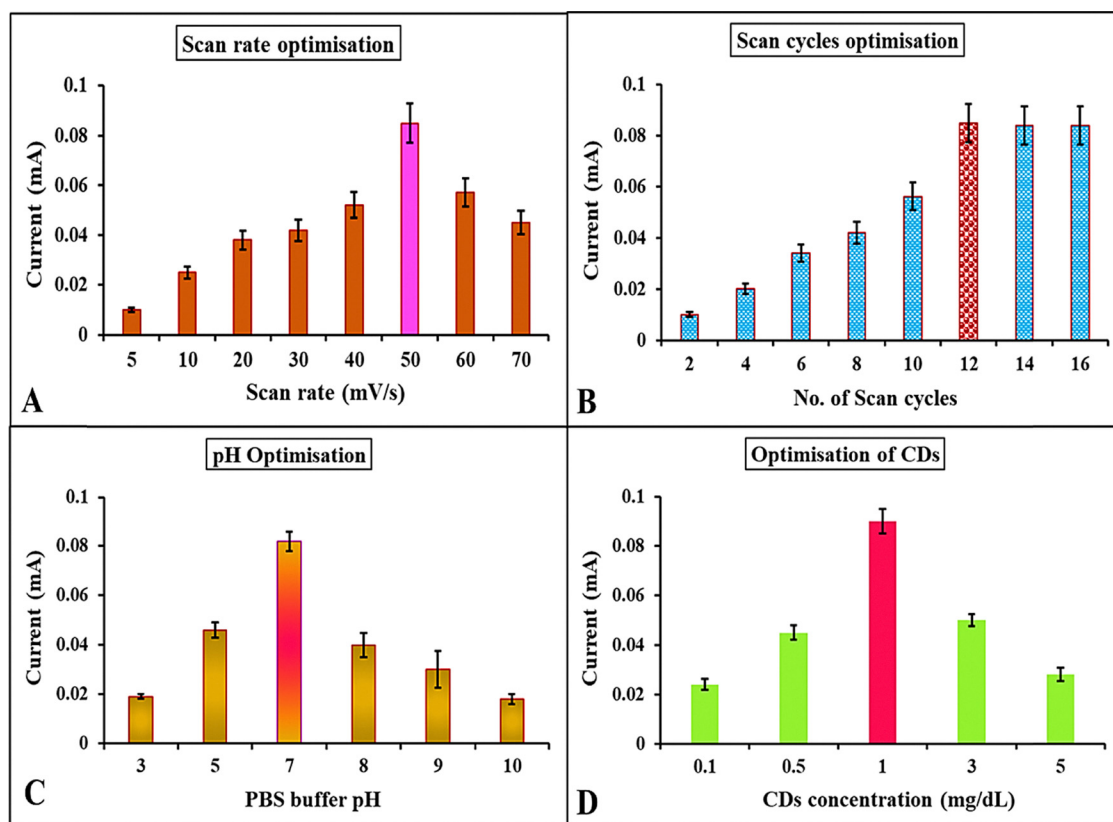

Fig. 5 Optimization of SPCE@MXene@CDs performance across four parameters: (A) scan rate, (B) number of scan cycles, (C) pH, and (D) CD concentration in 0.1 M PBS at pH 7.0. The error bars represent the standard deviation from triplicate measurements.

observations, electro-reduction of the SPCE@MXene@CDs layer was carried out using an optimized scan speed of 50 mV s^{-1}. The CV peak current was initially low (0.01–0.02 mA) during the initial scan cycles, followed by a significant rise at 12 cycles (0.09 mA), after which it stabilized (Fig. 5B). At fewer scan cycles, incomplete reduction of MXene and CDs resulted in lower conductivity and limited redox activity.[49] With an increase in the number of scan cycles, a uniform and well-reduced MXene@CDs layer was formed, enhancing the electron transfer efficiency. However, beyond 12 scan cycles, the electrode surface reached saturation, leading to a stable peak current. Next, the impact of pH on the CV performance was studied using SPCE@MXene@CDs at 50 mV s^{-1} scan speed, spanning 12 cycles (Fig. 5C). The CV peak current increased as the pH ranged from 3 to 7, indicating improved electron transfer and redox activity under near-neutral conditions. However, at pH levels above 7 (pH 8 to 10), a decline in the peak current was observed. This drop in peak current can be attributed to variations in proton availability and changes in the electrode surface charge, both of which impact the redox reaction efficiency. Based on these findings, pH 7 was identified as the optimal condition for further electrochemical studies. Finally, the variation in the peak current was investigated in response to variation in the CD concentration. The peak current showed an increase with CDs' concentration (0.1 and 1 mg dL^{-1}), as depicted in Fig. 5D. However, at concentrations beyond 1 mg dL^{-1}, a decline in peak current was observed. This drop can be linked to the development of a more substantial CD layer, which hinders electron transfer to the working electrode, thereby reducing the electrochemical efficiency.[48] Based on these findings, a CD concentration of 1 mg dL^{-1} was identified as the most suitable for subsequent experiments.

The CV analysis of SPCE@MXene showed a peak current of 0.02 A at 0.15 V (Fig. 6). In contrast, SPCE@MXene@CDs exhibited significantly enhanced redox peaks, with peak currents of 0.08 A and −0.07 A at 0.15 V and −0.13 V, respectively. The higher current feedback shows the successful integration of MXene and CDs, which provides additional active sites over the

SPCE and facilitates efficient redox reactions. These results indicate the superior electrochemical activity of SPCE@MXene@CDs compared to those of bare SPCE and SPCE@MXene, suggesting enhanced charge transfer kinetics and electrical conductivity. Herein, CDs enhance the conductivity of the SPCE by providing conductive pathways and improving electron transfer due to their sp^2-hybridized carbon structures.[50,51] The functional groups on CDs enhance interaction with the electrode and CR, reducing resistance. The large surface area of CDs offers more functional sites for electron exchange, lowering charge transfer resistance. CDs also accelerate electron transfer kinetics, reducing system impedance. Combined with MXene, they further improve conductivity, while ensuring uniform coating and consistent electrical pathways, ultimately enhancing the SPCE@MXene@CDs electrode's sensing performance.

3.3. Electrochemical detection of CR

CR sensing using the SPCE@MXene@CDs electrode was executed in 0.1 M PBS (pH 7) (Fig. 7A and B). The SPCE@MXene@CDs showed a considerably improved electrochemical response for CR, with a clear quasi-rectangular CV curve compared to the bare SPCE and SPCE@MXene (Fig. 7A). The current response of SPCE@MXene@CDs increased linearly with CR concentrations ranging from 0.001 to 5.0 mg dL^{-1}, along with an excellent correlation ($R^2 = 0.99$) (Fig. 7B). Triplicate measurements confirmed the reliability and reproducibility of the developed nanosensor, with a relative standard error of 1.8%. These results evidently demonstrate the robustness and consistent performance of the nanosensor for accurate CR detection. High reproducibility ensures that the SPCE@MXene@CDs sensor can deliver dependable results across multiple measurements, which is critical for practical and clinical applications. Henceforth, the SPCE@MXene@CDs sensor demonstrates superior performance in capturing and concentrating CR, thereby refining the accuracy of EC measurements. Furthermore, the deposition of CR molecules on the electrode surface facilitates redox processes, enhancing electron exchange between the molecules and the electrode.[48,52,53] Consequently, the increase in the current peak with higher CR concentrations is attributed to the greater number of EC interactions taking place between CR molecules and the SPCE@MXene@CDs-modified electrode surface. The enhanced electrochemical response arises from the synergistic effect of MXene's high conductivity and surface area with CDs' abundant functional groups and catalytic activity, which together accelerate electron transfer at the electrode–analyte interface. The carbonyl and imidazolidine nitrogen groups on CR can interact with the oxygenated and nitrogen-containing functional groups on CDs (–COOH, –OH, and –NH$_2$) through hydrogen bonding and coordination interactions.[54,55] Simultaneously, the –OH and –O terminations of MXene contribute additional hydrogen bonding and van der Waals interactions, facilitating strong adsorption and pre-concentration of CR molecules at the electrode surface. Under applied potential, these adsorbed molecules participate in efficient charge transfer processes, leading to enhanced current response. CDs provide abundant functional groups for molecular recognition and
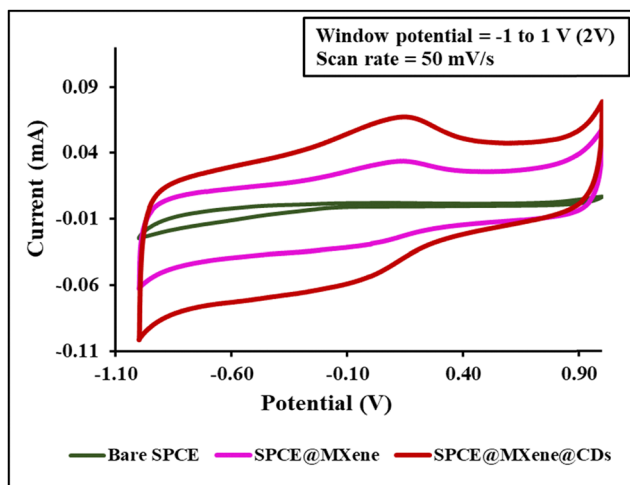
Fig. 6 CV characterization of bare SPCE, SPCE@MXene, and SPCE@MXene@CDs was performed in a 0.1 M PBS solution (pH 7) at a scan rate of 50 mV s^{-1}, using an Ag/AgCl reference electrode.
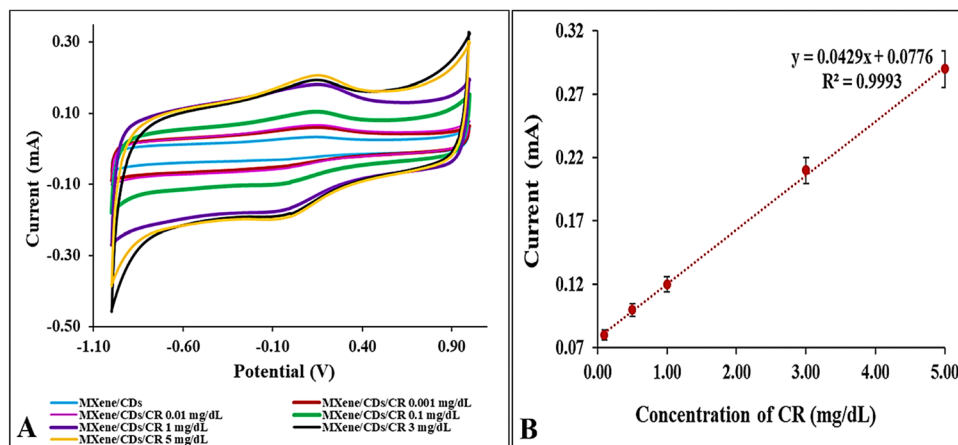
Fig. 7 Electrochemical characterization of SPCE@MXene@CDs in the presence of CR: (A) CV of SPCE@MXene@CDs recorded at various CR concentrations (0.001–5 mg dL^{-1}) along with blank SPCE@MXene@CDs (without CR) in 0.1 M PBS (pH 7) *versus* an Ag/AgCl reference electrode and (B) calibration plot demonstrating the current amplification of SPCE@MXene@CDs with increasing CR concentrations (0.001–5 mg dL^{-1}). Error bars in Fig. 7B denote the standard deviation of measurements from three independent replicates.

contribute to electron transfer through their conductive carbon framework, while MXene offers a high surface area, layered structure, and excellent electrical conductivity. Consequently, our method yielded improved sensitivity and precision towards CR detection. In contrast, the EC performance of SPCE@CR under identical CV conditions showed minimal enhancement in redox current signals (see Fig. S3). This minimal increase in current for SPCE@CR underscores the bare electrode's limited capability to produce a significant EC response for CR detection.

The stability of the fabricated SPCE@MXene@CDs sensor was crucial for assessing its suitability for practical CR detection. To evaluate its long-term performance, the modified electrode was stored at 4 °C and periodically analysed using CV, both in the absence and in the presence of CR. The results indicated that SPCE@MXene@CDs@CR maintained 97.8% of the initial redox peak current signals (Fig. S4A). This observation highlighted excellent stability and confirmed the reliability of the nanosensor

over this period. Beyond 15 days, a noticeable decline in current response was observed, suggesting the effective stability of the nanosensor to be *ca.* 15 days. The reproducibility of the nanosensor was further validated by repeating the SPCE@MXene@CDs@CR measurements four times under identical conditions (PBS (0.1 M, pH 7), 12 cycles, scan rate 50 mV s^{-1}, and potential range −1.0 to +1.0 V (Ag/AgCl)), as shown in Fig. S4B. The nearly overlapping responses confirm the excellent reproducibility and reliability of the fabricated electrode.

The DL for EC-based CR recognition was calculated to be 0.016 mg dL^{-1}, which is approximately 8–10 times lower than that of typical serum CR concentrations. A comparative analysis of our computed DL value with the reported literature is presented in Table 1. The five most proficient nanosensors with the lowest DL in the ascending order are listed below: SPCE@MXene@CDs (CR: 0.016 mg dL^{-1}) < Co-MOF-MXene@CB (CR: 0.056 mg dL^{-1}) < CuNPs (CR: 0.396 mg dL^{-1}) < CuO-IL/rGO modified electrode

Table 1 Overview of recently reported studies on EC sensing of CR, highlighting the LOD and LDR

S. no.	Nanostructured probe	Key biomarkers	Technique used	Detection range (mg dL^{-1})	Detection limit (mg dL^{-1})	Body fluid	Ref.
1	CuO-IL/rGO modified electrode	Creatinine	CV and amperometry	5.66–395.92	0.422	Human urine	56
2	GCE/SPCE@Potassium ferricyanide	Creatinine	CV	0.442–1.857	0.679	Human urine	57
3	ePAD	Creatinine	DPV	0.34–508.44	0.061	Human urine	58
4	CuNPs	Creatinine	CV	1.82–1.86	0.396	Human urine	59
5	SPCE@Carbon black@Fe^{3+}	Creatinine	CV and DPV	0.131–73.53	0.487	Human urine	60
6	SPCE@Cu$_2$O@MIP	Creatinine	Amperometry and EIS	0–11.312	0.249	Human urine	24
7	Pt-MEA	Creatinine	CV	0.00–56.56	0.75	Artificial urine	25
8	Co-MOF–MXene@CB	Creatinine	CV	0.00113–0.0905	0.0566	Human urine	58
9	Enzyme@CS/PB/MXene@AuNPs/SPCE	Creatinine	CV	0.339–45.25	0.113	Human urine, serum, and saliva	26
10	SPCE@MXene@CDs	Creatinine	CV	0.01–1	0.016	Human serum	Current work

Abbreviations: Cu-CNF/ACF: copper-carbon nanofiber/activated carbon fiber; AgNPs: silver nanoparticles; CNT: carbon nanotube; CPE: carbon paste electrode; FA: folic acid; CuNPs: copper nanoparticles; CV: cyclic voltammetry; rGO: reduced graphene oxide; GCE: glassy carbon electrode; Pd/Cu$_2$O/PPy: palladium/cuprous oxide/polypyrrole; SPCE: screen printed carbon electrode; Pt-MEA: platinum-microelectrode array; Co-MOF–MXene@CB: cobalt-metal organic framework–MXene@carban black; CS: chitosan; PB: Prussian blue; AuNPs: gold nanoparticles; DPV: differential pulse voltammetry; MIP: molecularly imprinted polymer; and EIS: electrochemical impedance spectroscopy.

(CR: 0.422 mg dL^{-1}) < Pt-MEA (CR: 0.75 mg dL^{-1}). The DL of our nanosensor was the lowest among those in the compared studies, underscoring its remarkable sensitivity for detecting and quantifying CR at very low concentrations. Additionally, we compared the DR of our nanosensor with those reported in the literature to further assess its performance. A nanosensor with a broad DR offers greater versatility by accurately measuring a wide range of analyte concentrations. It enhances sensitivity and accuracy, allowing for detailed analysis and easier calibration. The five most leading nanosensors with regards to DR parameter in decreasing order are as follows: SPCE@MXene@CDs nanosensor (CR: 0.01–1 mg dL^{-1}) > Enzyme@CS/PB/MXene@AuNPs/SPCE (CR: 0.339–45.25 mg dL^{-1}) > Co-MOF–MXene@CB (CR: 0.00113–0.0905 mg dL^{-1}) > SPCE@Cu$_2$O@MIP (CR: 0–11.31 mg dL^{-1}) > CuNPs (CR: 1.82–1.86 mg dL^{-1}). The broad DR of our nanosensor guarantees consistent performance across diverse sample conditions and concentration levels.

To evaluate the selectivity of CR detection, specificity studies were performed with physiological concentrations of possible biochemical interferents, comprising GSH, globulin, bilirubin, gentamicin, vancomycin, arginine, histidine, AA, glucose, BSA, urea, Ca^{2+}, Mg^{2+}, SO$_4^{2-}$, and K$^+$. These biomolecules were selected on the basis of their co-existence with CR in body fluids. These interfering substances caused a negligible increase in the redox current of the SPCE@MXene@CDs (Fig. 8). The substantial increase in current signals was observed solely in the presence of CR, highlighting the exceptional specificity of the developed nanosensor towards CR identification.

The clinical applicability of the SPCE@MXene@CDs sensor was evaluated using serum samples collected from normal subjects and individuals diagnosed with CKD. When tested with 89 serum samples containing known CR concentrations (see Table S1), the nanosensor showed significant enhancement in current signals. Importantly, the CKD cohort displayed substantial clinical diversity. Early-stage patients (stages 1–2) were primarily associated with hypertension, while those in stages 3–4 frequently presented with additional complications such as cardiac issues, neurological disorders, anaemia, and endocrine abnormalities (e.g., hyperthyroidism). The largest subset was stage 5 patients on dialysis, who exhibited a wide spectrum of comorbidities, including hypertension, cardiovascular diseases, diabetes, anaemia, neuropathy, cognitive dementia, hyperthyroidism, and dyslipidaemia. Notably, even complex conditions such as diabetic foot ulcer, paralysis, and heart failure were represented. Our nanosensor displayed an indistinguishable response for CR detection across the diverse patient cohort. This exceptional performance underscores the robustness and reliability of the fabricated nanosensor in detecting CR levels irrespective of CKD severities, highlighting its strong potential for real-world diagnostic applications. Our method for measuring CR concentrations yielded observations that closely matched those obtained using the clinically validated Jaffe method (see Table S1). Bland–Altman and scatter plot analyses (see Fig. S5) demonstrated a high degree of correlation (R^2 = 0.99) relative to the Jaffe method, further confirming the reliability of the nanosensor for CR analysis. CR concentrations measured by both approaches showed excellent concordance, with only minor variations across samples (generally <3%). Out of 89 samples, 81 were true positives, 6 were true negatives, and only 2 showed slight deviations, recorded as false negatives (7.11% and 8.76%). The close agreement with the Jaffe method highlights the reliability, sensitivity, and clinical applicability of the proposed nanosensor for CR detection in human serum. The ability of the nanosensor to detect CR in micro-volumes (5 µL) of serum makes it a promising tool for minimally invasive and point-of-care (POC) applications. It reduces the discomfort associated with large blood samples, speeds up testing procedures, and makes POC testing more feasible by enabling tests at or near the patient's location. This capability lowers costs, enhances patient compliance, and allows for more frequent monitoring of
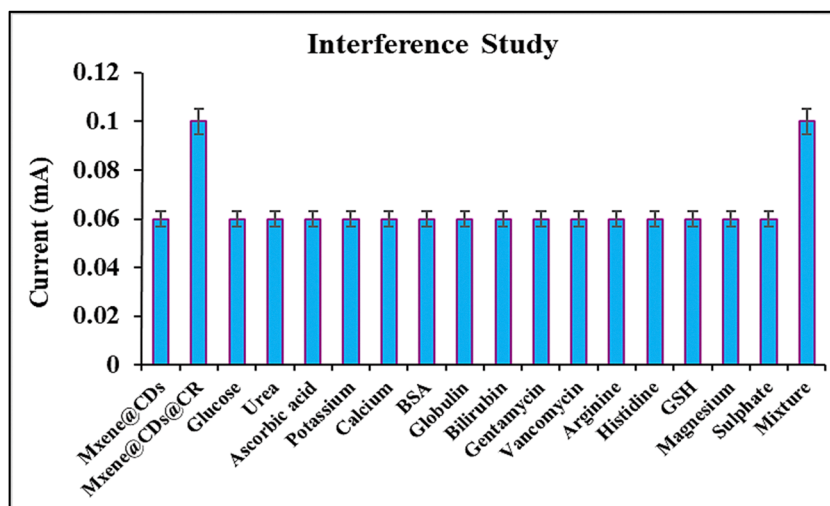

Fig. 8   Selectivity of SPCE@MXene@CDs for CR in the presence of various interfering biomolecules.

chronic conditions, ultimately improving diagnostic efficiency and patient care.

A comparative statistical analysis was performed to evaluate the agreement between the electrochemical method and the standard Jaffe approach for CR quantification. The paired t-test yielded a test statistic of -1.11 with a corresponding p-value of 0.272, indicating no statistically significant difference between the two methods ($p > 0.05$). The mean difference in CR concentration was -0.0128 mg dL^{-1}, and the 95% confidence interval for this difference ranged from -0.0359 to $+0.0102$ mg dL^{-1}. Since the confidence interval is zero with negligible mean bias, the results confirmed excellent concordance between the developed electrochemical assay and the Jaffe method. This statistical finding is in strong agreement with the Bland–Altman analysis (Fig. S5), which further validates the reliability and clinical applicability of the developed nanosensor.

4. Conclusion

An innovative EC nanosensor, incorporating SPCE@MXene@CDs, was developed for the highly accurate detection of CR in PBS as well as in human serum obtained from healthy participants and individuals diagnosed with CKD. The integration of SPCE@MXene@CDs significantly amplified EC redox signals for CR, achieving a DL of 0.016 mg dL^{-1} with notable sensitivity and the capability to work with ultra-low sample volumes (5 μL). The electrical conductivity of SPCE@MXene@CDs was improved by carefully adjusting the scan rate, number of scan cycles, buffer pH, and concentration of CDs. The nanosensor demonstrated excellent selectivity, with no notable interference from common metabolites such as glucose, urea, AA, GSH, BSA, globulin, bilirubin, gentamicin, vancomycin, arginine, and histidine and key electrolytes (Ca^{2+}, Mg^{2+}, PO_4^{3-}, and SO_4^{2-}), confirming its high specificity. The SPCE@MXene@CDs-based sensor demonstrated a strong correlation with the standard Jaffe method ($R^2 = 0.99$) for CR quantification in human serum samples ($n = 89$) and exhibited excellent agreement, with a negligible mean difference (-0.0128 mg dL^{-1}) and a 95% confidence interval of -0.0359 to $+0.0102$ mg dL^{-1} ($p = 0.272$). These outcomes highlight the nanosensor's reliability and accuracy in complex biological environments, positioning it as a minimally invasive and highly effective tool for rapid CR monitoring, with the potential to enhance patient adherence and clinical outcomes.

Conflicts of interest

There are no conflicts to declare.

Data availability

The raw data is provided separately as an MS-excel file along with the manuscript.

Supplementary information (SI) is available. See DOI: https://doi.org/10.1039/d5ma00539f.

Acknowledgements

References

1 K. Kalantar-Zadeh, T. H. Jafar, D. Nitsch, B. L. Neuen and V. Perkovic, *Lancet*, 2021, **398**, 786–802.

2 P. Cockwell and L.-A. Fisher, *Lancet*, 2020, **395**, 662–664.

3 B. L. Neuen, S. J. Chadban, A. R. Demaio, D. W. Johnson and V. Perkovic, *BMJ Global Health*, 2017, **2**, e000380.

4 B. L. Neuen, A. K. Bello, A. Levin, M. Lunney, M. A. Osman, F. Ye, G. E. Ashuntantang, E. Bellorin-Font, M. B. Gharbi and S. Davison, *PLOS Global Public Health*, 2023, **3**, e0001467.

5 N. Promphet, S. Akgönüllü, C. Moonla, P. Nandhakumar, P. Tanglertsampan, T. Laochai, N. Laichuthai, J. Wang and N. Rodthongkum, *Sens. Actuators, B*, 2025, **441**, 137967.

6 H. Shahbaz and M. Gupta, in *StatPearls*, StatPearls Publishing, 2023.

7 K. Sumida, G. N. Nadkarni, M. E. Grams, Y. Sang, S. H. Ballew, J. Coresh, K. Matsushita, A. Surapaneni, N. Brunskill and S. J. Chadban, *Ann. Intern. Med.*, 2020, **173**, 426–435.

8 Z. Saddique, N. Shahzad, M. Saeed and A. Afzal, *ACS Appl. Bio Mater.*, 2025, **8**, 4262–4271.

9 K. Kashani, M. H. Rosner and M. Ostermann, *Eur. J. Intern. Med.*, 2020, **72**, 9–14.

10 K. Kaewket, T. C. R. Outrequin, S. Deepaisarn, J. Wijitsak, P. Sunon and K. Ngamchuea, *ACS Sens.*, 2025, **10**, 3471–3483.

11 T. Küme, B. Sağlam, C. Ergon and A. R. Sisman, *J. Clin. Lab. Anal.*, 2018, **32**, e22168.

12 H. Husdan and A. Rapoport, *Clin. Chem.*, 1968, **14**, 222–238.

13 K. Boss, S. Stolpe, A. Müller, J. Friebus-Kardash, B. Wagner, M. Wichert, R. Assert, L. Volbracht, A. Stang and B. Kowall, *J. Clin. Med.*, 2024, **13**, 6066.

14 M. Yildirimel, M. N. Atalar, S. Abusoglu, D. Eryavuz Onmaz, A. Sivrikaya, G. Abusoglu and A. Unlu, *Turk. J. Biochem.*, 2021, **46**, 263–271.

15 C. L. Gonzalez-Gallardo, N. Arjona, L. Álvarez-Contreras and M. Guerra-Balcázar, *RSC Adv.*, 2022, **12**, 30785–30802.

16 S. N. Prabhu, S. C. Mukhopadhyay and G. Liu, *IEEE Sens. J.*, 2022, **22**, 11427–11438.

17 R. K. R. Kumar, M. O. Shaikh and C.-H. Chuang, *Anal. Chim. Acta*, 2021, **1183**, 338748.

18 E. E. Elemike, J. Adeyemi, D. C. Onwudiwe, L. Wei and A. O. Oyedeji, *J. Energy Storage*, 2022, **50**, 104711.

19 S. K. Bhardwaj, H. Singh, M. Khatri, K.-H. Kim and N. Bhardwaj, *Biosens. Bioelectron.*, 2022, **202**, 113995.

20 H. Zhang, Z. Wang, Q. Zhang, F. Wang and Y. Liu, *Biosens. Bioelectron.*, 2019, **124**, 184–190.

21 Y.-J. Du, J. Yang, Z. Lv, Y. Zhai, Z. Yi, Y. Xie, M.-L. Zheng, X. Ma, G. Gong, Y. Wang, Y. Zhou and S.-T. Han, *Adv. Funct. Mater.*, 2025, **35**, 2500953.

22 Y. Zhai, G. Duan, J. Hu, Z. Lv, G. Ding, Y. Zhou and S.-T. Han, *Adv. Funct. Mater.*, 2024, **34**, 2406239.

23 L. Guo, H. Han, J. Wang, P. Wang, C. Du, B. Wang, Q. Yuan, Y. Zhai and C. Zhang, *J. Mater. Chem. A*, 2024, **12**, 20414–20424.

24 S. Nur Ashakirin, M. H. M. Zaid, M. A. S. M. Haniff, A. Masood and M. F. Mohd Razip Wee, *Measurement*, 2023, **210**, 112502.

25 K. Kaewket and K. Ngamchuea, *RSC Adv.*, 2023, **13**, 33210–33220.

26 Y. Li, Y. Hang, R. Gopali, X. Xu, G. Chen, X. Guan, N. Bao and Y. Liu, *Microchim. Acta*, 2024, **191**, 534.

27 D. Roy, R. Singh, S. Mandal and N. Chanda, *Anal. Methods*, 2024, **16**, 6183–6192.

28 Y. Li, X. Zhong, A. E. Rider, S. A. Furman and K. (Ken) Ostrikov, *Green Chem.*, 2014, **16**, 2566–2570.

29 Q. Liu, N. Zhang, H. Shi, W. Ji, X. Guo, W. Yuan and Q. Hu, *New J. Chem.*, 2018, **42**, 3097–3101.

30 P. Bhatt, D. Kukkar and A. K. Yadav, *Microchim. Acta*, 2024, **191**, 1–12.

31 A. Thakur, N. B. S. Chandran, K. Davidson, A. Bedford, H. Fang, Y. Im, V. Kanduri, B. C. Wyatt, S. K. Nemani, V. Poliukhova, R. Kumar, Z. Fakhraai and B. Anasori, *Small Methods*, 2023, **7**, 2300030.

32 K. P. Loh, *Chem. Mater.*, 2023, **35**, 8771–8773.

33 X. Y. Sun, M. J. Yuan, B. Liu and J. S. Shen, *RSC Adv.*, 2018, **8**, 19786–19790.

34 J. Wu, X. Chen, Z. Zhang and J. Zhang, *Microchim. Acta*, 2022, **189**, 131.

35 D. A. Armbruster and T. Pry, *Clin. Biochem. Rev.*, 2008, **29**(Suppl 1), S49–S52.

36 M. Zaib, A. Akhtar, F. Maqsood and T. Shahzadi, *Arabian J. Sci. Eng.*, 2021, **46**, 437–446.

37 J. Ren, F. Weber, F. Weigert, Y. Wang, S. Choudhury, J. Xiao, I. Lauermann, U. Resch-Genger, A. Bandea and T. Petit, *Nanoscale*, 2019, **11**, 2056–2064.

38 H. Shibata, M. Abe, K. Sato, K. Uwai, K. Tokuraku and T. Iimori, *Carbohydr. Polym. Technol. Appl.*, 2022, **3**, 100218.

39 P. Bhatt, D. Kukkar, A. K. Yadav and K.-H. Kim, *Spectrochim. Acta, Part A*, 2024, **307**, 123666.

40 W. Cao, J. Nie, Y. Cao, C. Gao, M. Wang, W. Wang, X. Lu, X. Ma and P. Zhong, *Chem. Eng. J.*, 2024, **496**, 154097.

41 H. Fang, Z. Fang, A. Thakur, B. Anasori, A. M. Rappe and Z. Fakhraai, *J. Phys. Chem. Lett.*, 2025, **16**, 7515–7521.

42 M. Lounasvuori, Y. Sun, T. S. Mathis, L. Puskar, U. Schade, D.-E. Jiang, Y. Gogotsi and T. Petit, *Nat. Commun.*, 2023, **14**, 1322.

43 T. Parker, D. Zhang, D. Bugallo, K. Shevchuk, M. Downes, G. Valurouthu, A. Inman, B. Chacon, T. Zhang, C. E. Shuck, Y.-J. Hu and Y. Gogotsi, *Chem. Mater.*, 2024, **36**, 8437–8446.

44 T. Cygan, J. Wozniak, M. Petrus, A. Lachowski, W. Pawlak, B. Adamczyk-Cieślak, A. Jastrzębska, A. Rozmysłowska-Wojciechowska, T. Wojciechowski, W. Ziemkowska and A. Olszyna, *Materials*, 2021, **14**(4), 829.

45 D. Liu, T. Li, W. Sun, W. Zhou and G. Zhang, *ACS Omega*, 2022, **7**, 31945–31953.

46 T. Hu, J. Wang, H. Zhang, Z. Li, M. Hu and X. Wang, *Phys. Chem. Chem. Phys.*, 2015, **17**, 9997–10003.

47 A. T. Smith, A. M. LaChance, S. Zeng, B. Liu and L. Sun, *Nano Mater. Sci.*, 2019, **1**, 31–47.

48 J. I. A. Rashid, V. Kannan, M. H. Ahmad, A. A. Mon, S. Taufik, A. Miskon, K. K. Ong and N. A. Yusof, *Mater. Sci. Eng., C*, 2021, **120**, 111625.

49 P. M. Nia, H. S. Jenatabadi, P. M. Woi, E. Abouzari-Lotf and Y. Alias, *Measurement*, 2019, **137**, 683–690.

50 C. F. Jones, L. Resina, F. C. Ferreira, P. Sanjuan-Alberte and T. Esteves, *J. Phys. Chem. C*, 2024, **128**, 11083–11100.

51 L. Mishra, R. K. Behera, S. Mondal, A. Panigrahi and M. K. Sarangi, *J. Phys. Chem. C*, 2021, **125**, 23398–23408.

52 R. B. Jadhav, T. Patil and A. P. Tiwari, *Appl. Surf. Sci. Adv.*, 2024, **19**, 100567.

53 M. J. Pedrozo-Peñafiel, T. Lópes, L. M. Gutiérrez-Beleño, M. E. H. M. Da Costa, D. G. Larrudé and R. Q. Aucelio, *J. Electroanal. Chem.*, 2020, **878**, 114561.

54 S. Kainth, B. Maity and S. Basu, *RSC Adv.*, 2020, **10**, 36253–36264.

55 M. Fu, Z. Feng, J. Wang, Y. Zhu, L. Gan and X. Yang, *Appl. Surf. Sci.*, 2022, **571**, 151298.

56 K. Teekayupak, C. Aumnate, A. Lomae, P. Preechakasedkit, C. S. Henry, O. Chailapakul and N. Ruecha, *Talanta*, 2023, **254**, 124131.

57 S. Bajpai, G. R. Akien and K. E. Toghill, *Electrochem. Commun.*, 2024, **158**, 107624.

58 R. Manikandan, J.-H. Yoon, J. Lee and S.-C. Chang, *Microchem. J.*, 2024, **204**, 111114.

59 K. Ngamchuea, S. Wannapaiboon, P. Nongkhunsan, P. Hirunsit and I. Fongkaew, *J. Electrochem. Soc.*, 2022, **169**, 20567.

60 E. L. Fava, T. M. do Prado, A. Garcia-Filho, T. A. Silva, F. H. Cincotto, F. Cruz de Moraes, R. C. Faria and O. Fatibello-Filho, *Talanta*, 2020, **207**, 120277.